Low-complexity generalized coherence factor estimated from binarized signals in ultrasound beamforming

Masanori Hisatsu[1,2] · Shohei Mori[3] · Mototaka Arakawa[2,3] · Hiroshi Kanai[2,3]

Abstract

Purpose In coherence-based beamforming (CBB) using a generalized coherence factor (GCF), unnecessary signals caused by sidelobes are reduced, and an excellent contrast-to-noise ratio (CNR) is achieved in ultrasound imaging. However, the GCF computation is complex compared to the standard delay-and-sum (DAS) beamforming. In the present study, we propose a method that significantly reduces the number of GCF computations.

Methods In the previously proposed GCF$_{real}$, generation of the analytic signal for each element in the conventional GCF could be omitted. Furthermore, in GCF estimated from binarized signals (GCFB) proposed in the present study, the GCF value is calculated after the received signal of each element is binarized to reduce the computational complexity of the GCF.

Results The values of GCFB and GCF$_{real}$ estimated from simulation and experimental data were compared. We also evaluated the image quality of B-mode images weighted by GCFB and GCF$_{real}$. Compared with GCF$_{real}$, GCFB was superior in reducing unnecessary signals but tended to reduce the brightness of the diffused scattering media. The CNR improvement was comparable for both methods.

Conclusion Generalized coherence factor estimated from binarized signals exhibits excellent CNR improvement compared to DAS. CNR improvements yielded by GCFB and GCF$_{real}$ may depend on the observation target; however, under the conditions of the present study, comparable performances were obtained. Because GCFB can significantly reduce the computational complexity, it is potentially applicable in clinical diagnostic equipment.

Keywords Ultrasound imaging · Adaptive beamforming · Generalized coherence factor

Introduction

In delay-and-sum (DAS) beamforming, which is the standard beamforming technique for medical ultrasound imaging, signal components from undesired positions remain because of sidelobe components. These unnecessary signals cause artifacts and contrast degradation in B-mode images. Apodization, which weights a preset window function to the received signals of individual elements, is applied as a general method to reduce the sidelobe components at the

expense of lateral resolution and signal-to-noise ratio (SNR) [1]. Generally, apodization is not applied (set the weights of all elements to 1) in the deep region to prevent SNR degradation.

Numerous adaptive beamforming techniques have been proposed to reduce the unnecessary signals contained in received signals [2–4]. Coherence-based beamforming (CBB) [5–12], which is one of the techniques, is effective in reducing unnecessary signals caused by sidelobes with low computational complexity. In CBB, the coherence factor (CF) [5, 13, 14], which represents the coherence among the received signals, is weighted to the signal after DAS to reduce the brightness value of the pixel where the unnecessary signal is dominant.

Speckle noises [15, 16] are generated in B-mode images of the human body owing to the interference of sound waves from many scatterers. Speckle noise is a variation of the brightness value that is not directly related to the structure in the human body. In ultrasound diagnosis, lesions are often

✉ Masanori Hisatsu
 masanori.hisatsu.uc@fujifilm.com

1 FUJIFILM Healthcare Corporation, 3-1-1 Higashikoigakubo, Kokubunji, Tokyo 185-0014, Japan

2 Graduate School of Biomedical Engineering, Tohoku University, Sendai, Miyagi 980-8579, Japan

3 Graduate School of Engineering, Tohoku University, Sendai, Miyagi 980-8579, Japan

observed from minute changes in brightness, and the speckle noises interfere with diagnosis by lowering the contrast-to-noise ratio (CNR) [17]. When applying CBB, it is necessary to focus on the CNR as well as the effect of reducing unnecessary signals. The generalized coherence factor (GCF) [6, 7, 18], which is one of the factors used for CBB, focuses on the depiction of diffused scattering media, and has a significantly better CNR than other factors [19].

Recently, high-performance beamforming techniques including CBB have been realized in real time by improving the performance of field-programmable gate arrays (FPGA), central processing units (CPUs), and graphics processing units (GPUs) [20, 21]. The synthetic transmit aperture (STA) [22–27] technique, which realizes dynamic-transmit focusing, can also be realized with commercial ultrasonic diagnostic equipment. However, the STA technique requires dozens of times more DAS processing for each transmission. Therefore, a technology with a lower computational complexity is required to incorporate CBB into the STA. In contrast, ultrasonic diagnostic equipment has been made smaller and more portable. To achieve high image quality with limited computing power for such a model, it is necessary to reduce the computational complexity of CBB, making it possible to expand the image quality with a wider range of models.

The aim of this study is to reduce the computational complexity of the GCF [6], which has better CNR than other factors used in CBB. With the GCF, it is necessary to generate an analytic signal for the received signal of each element and perform a discrete Fourier transform (DFT) in the element direction at each sample point. Therefore, the computational complexity is high compared to the standard DAS beamformer. We have shown in a previous study [28] that generation of the analytic signals can be omitted, and the GCF value can be calculated from real signals. In the present study, we propose a method that further reduces the computational complexity of the GCF value calculation by binarizing the real input signals. Moreover, the performance difference between the proposed method and conventional GCF is verified, and the validity of the proposed method is evaluated.

Conventional methods

Figure 1a shows the system block diagram for CBB using GCF. The focused beam is generated from received signals in the number of channels connected to the ultrasound diagnostic apparatus. The received signals in the channels are converted to digital signals discretized in the time direction by analog-to-digital converters (ADC) and delayed to in phase for waves from the focus point. The GCF is calculated from the received signals after delay processing and before summation, and then used as a weighting value for the

signal $x_{in}(n, l)$ after applying DAS [6]. Here, n is the sample number in the time direction and l is the scan line number. By weighting the GCF value to the signal $x_{in}(n, l)$, $x_{in}(n, l)$ including unnecessary signals is suppressed and output as a signal $x_{out}(n, l)$. This process is applied at each focus point corresponding to (n, l) and repeated at all positions. However, as the GCF decreases to a very small value around the strong scatterer, the brightness of the surrounding diffused scattering medium is significantly reduced, and a dark region artifact (DRA) is generated [29]. Therefore, to apply GCF to a B-mode image, it is necessary to adjust the reduction effect. In the present study, similar to the sign coherence factor (SCF) [8], the index p in Eq. (1) was used as the weight:

$$x_{out}(n, l) = [GCF(n, l)]^p x_{in}(n, l). \tag{1}$$

Adjustment by the power p is implemented using a look-up table (LUT), as outlined in Fig. 1a. If $p < 1$ is set to weaken the reduction effect in DRA, the relationship between $GCF(n, l)$ and $[GCF(n, l)]^p$ is as shown in Fig. 1b.

Calculation of the GCF value is described next. When the analytic signal generated from the received signal of the channel number $m(m = 0, 1, \cdots, M - 1)$ is represented by $I(m, n, l) + jQ(m, n, l)$, the GCF is calculated from Eq. (2) using the Fourier coefficient $S_{IQ}(k, n, l)$ obtained by the DFT of $I(m, n, l) + jQ(m, n, l)$ in the m-th direction [6]:

$$GCF(n, l; K_0) = \frac{\sum_{k=-K_0}^{K_0} \left| S_{IQ}(k, n, l) \right|^2}{M \cdot \sum_{m=0}^{M-1} |I(m, n, l) + jQ(m, n, l)|^2}, \tag{2}$$

where k is the frequency index in the m-th direction, and $k = -K, -K + 1, \ldots, 0, \ldots, K - 1, (K = M/2)$ for an even number M. The GCF value is the ratio of the power value of all frequency components (denominator) to that of the DC vicinity components represented by $[-K_0, K_0]$ (numerator). Figure 2a shows the block diagram for calculating the GCF value using Eq. (2). Generation of the analytic signal in each channel requires processing such as mixers and filters at a high sampling frequency in the n-th direction. Therefore, when these processes are applied to all the channel signals, the computational complexity increases significantly. Therefore, we proposed a method for calculating the GCF value from real signals without generating analytic signals [28]. When generation of the analytic signal is omitted and the GCF value is calculated from the real signals, a frequency component that is twice the frequency of the received signal is generated in the n-th direction. It was demonstrated that GCF_{real} obtained by removing this component using a low-pass filter (LPF) was equivalent to the GCF in Eq. (2). In Eq. (2), replacing the analytic signal $I(m, n, l) + jQ(m, n, l)$ with the real signal $s(m, n, l)$, and $S_{IQ}(k, n, l)$ with $S(k, n, l)$,
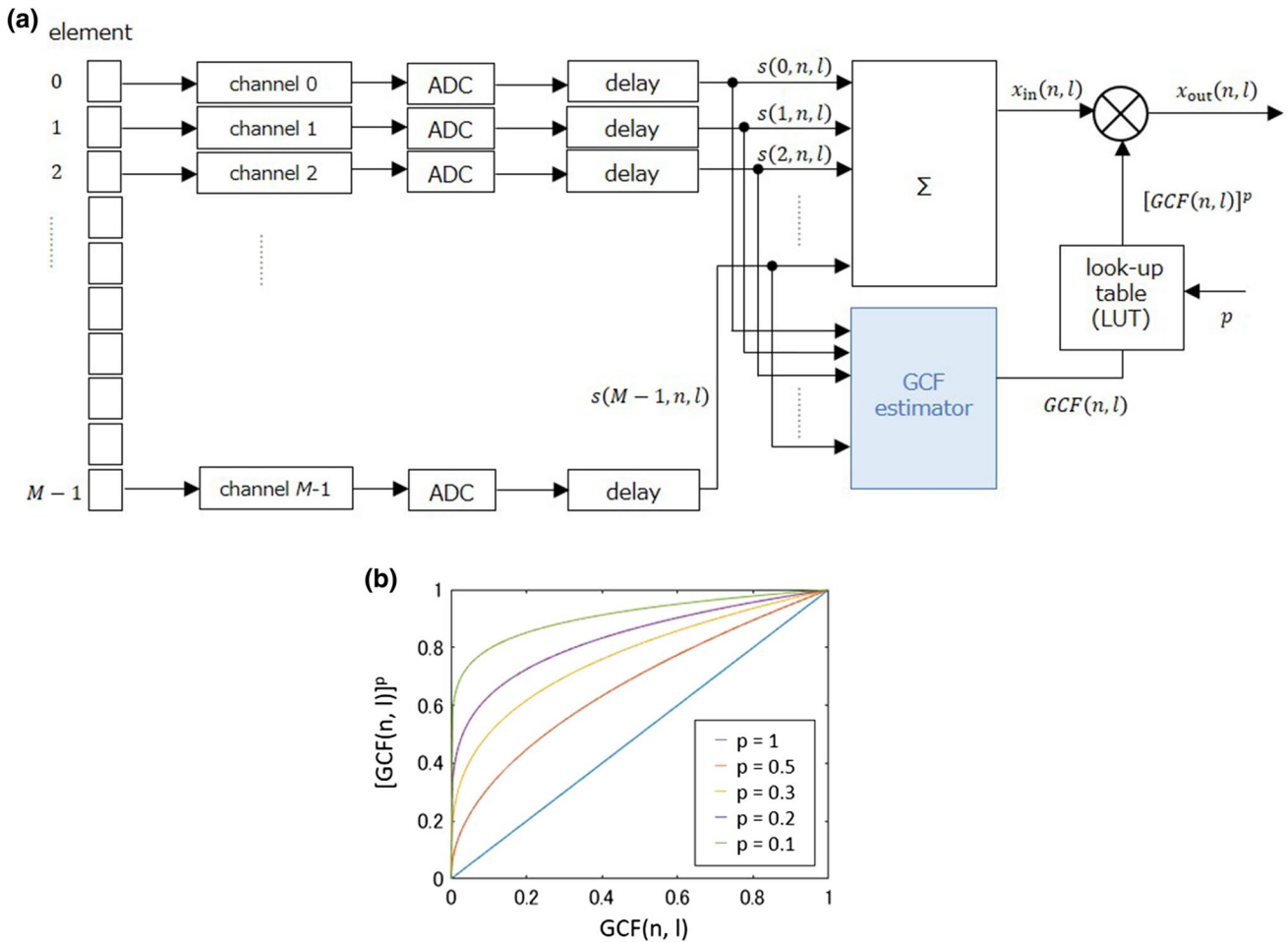
Fig. 1 **a** System block diagram for coherence-based beamforming and **b** input/output of the LUT

then adding LPFs to the numerator and denominator in the n-th direction, GCF_{real} is expressed as

$$GCF_{real}(n,l;K_0) = \frac{\sum_{h=-N_f}^{N_f}\left[f_{LPF}(h) \cdot \left\{\sum_{k=-K_0}^{K_0}|S(k,n-h,l)|^2\right\}\right]}{\sum_{h=-N_f}^{N_f}\left[f_{LPF}(h) \cdot \left\{M\sum_{m=0}^{M-1}|s(m,n-h,l)|^2\right\}\right]}.$$

(3)

Equation (3) shows the case where a finite impulse response low-pass filter (FIR-LPF) with coefficients $f_{LPF}(h), (h = -N_f \ldots N_f)$ is used as the LPF.

Generalized coherence factor estimated from binarized signals (GCFB)

In the present study, we propose a method that further reduces the computational complexity of Eq. (3), which calculates the GCF value without the generation of analytic signals. The input real signal $s(m,n,l)$ is binarized as

$$u(m,n,l) = \begin{cases} -1 & \text{if } s(m,n,l) < 0, \\ +1 & \text{if } s(m,n,l) \geq 0, \end{cases}$$

(4)

and the DFT for $u(m,n,l)$ in the m-th direction is given by

$$U(k,n,l) = \sum_{m=0}^{M-1} u(m,n,l)\exp\left[-j\frac{2mk\pi}{M}\right].$$

(5)

Because $u(m,n,l)$ is 1 or -1, Eq. (5) can be calculated by adding and subtracting complex exponential functions. Replacing the real signal $s(m,n,l)$ with the binary signal $u(m,n,l)$, and $S(k,n,l)$ with $U(k,n,l)$, Eq. (3) is expressed as

$$GCFB(n,l;K_0) = \frac{\sum_{h=-N_f}^{N_f}\left[f_{LPF}(h) \cdot \left\{\sum_{k=-K_0}^{K_0}|U(k,n-h,l)|^2\right\}\right]}{\sum_{h=-N_f}^{N_f}\left[f_{LPF}(h) \cdot \left\{M\sum_{m=0}^{M-1}|u(m,n-h,l)|^2\right\}\right]}.$$

(6)

The denominator is a fixed value because $|u(m,n,l)|^2 = 1$, so LPF can be omitted, and Eq. (6) becomes

(a)

(b)

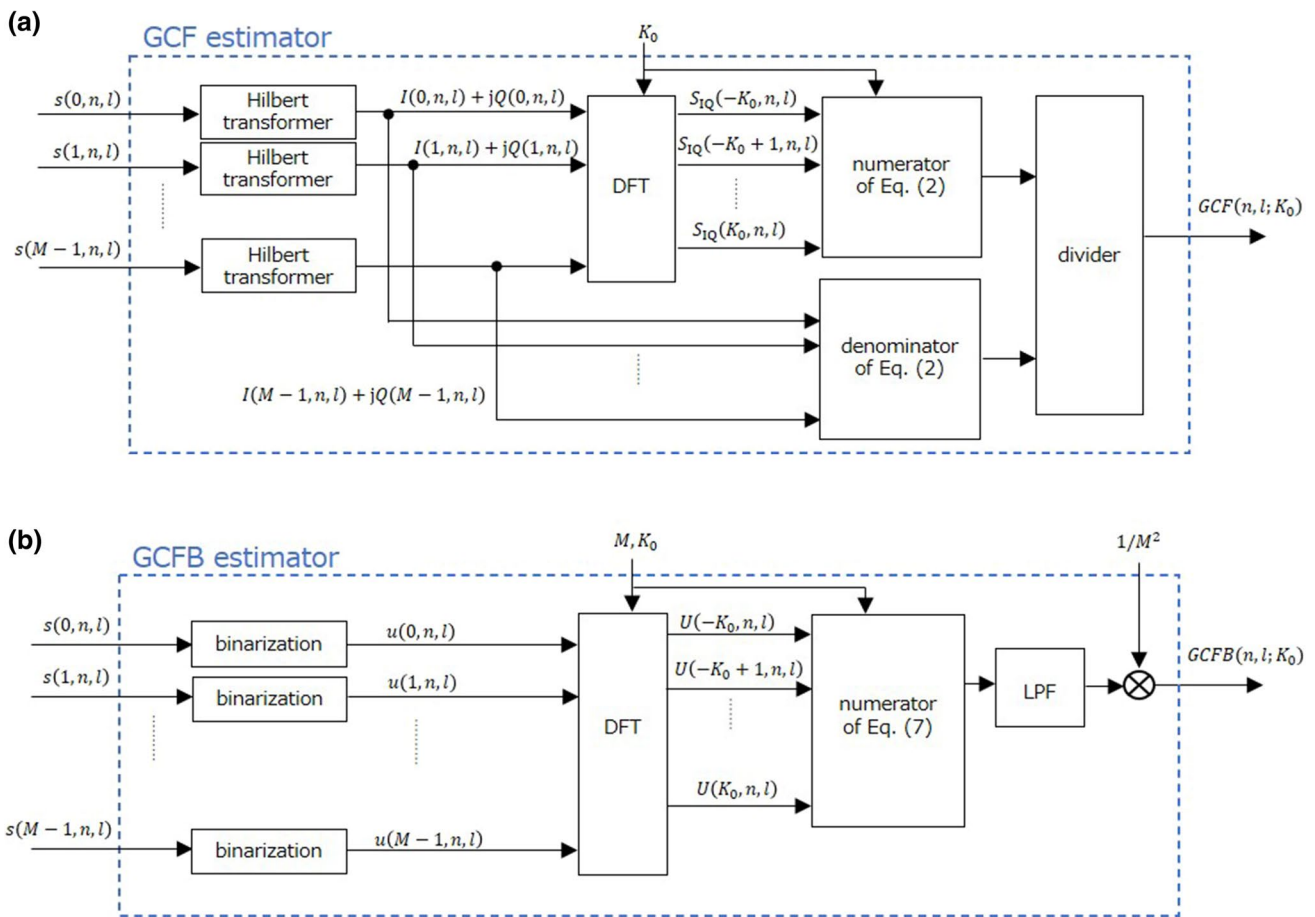
Fig. 2 System block diagram for **a** conventional GCF and **b** GCFB estimators

$$GCFB(n, l; K_0) = \frac{\sum_{h=-N_f}^{N_f} \left[f_{\text{LPF}}(h) \cdot \left\{ \sum_{k=-K_0}^{K_0} |U(k, n-h, l)|^2 \right\} \right]}{M^2}.$$

(7)

The computational complexity of GCFB can be reduced compared to GCF_{real} because (1) the DFT of Eq. (5) can be calculated only by addition and subtraction, (2) the addition and LPF of the denominator in Eq. (6) can be omitted, and (3) the division of Eq. (7) can be replaced with multiplication of the fixed value $1/M^2$. The configuration for calculating the GCFB from Eq. (7) is shown in Fig. 2b, which is simpler than the configuration of the conventional GCF shown in Fig. 2a.

Comparison of computational load of conventional GCF, GCF$_{\text{real}}$, and GCFB

Table 1 shows the number of multiplications and additions required to calculate the GCF, GCF_{real}, and GCFB values for each spatial sample. Here, it is assumed that the order $2N_f$ of the Hilbert transform filter required in the conventional GCF is similar to the order of the LPF

used in Eq. (3) or Eq. (7). For GCF_{real} and GCFB, the frequency components were calculated only on the positive side because the frequency spectrum of a real signal is positive–negative symmetric. To demonstrate the calculation complexity of each method, an example where the channel number $M = 96$, DC vicinity range $K_0 = 1$, and Hilbert transform or LPF order $2N_f = 20$ is shown. For GCF_{real}, the number of multiplications and additions is approximately 1/6 of those for GCF. Furthermore, for GCFB, the number of multiplications is 1/20 or less of those for GCF_{real}. For GCFB, the calculation complexity can be further reduced by replacing the division in Eq. (7) with multiplication of $1/M^2$. Especially in ASICs and FPGAs, the circuit scale can be condensed by reducing the number of such operations. However, reduction of the calculation depends on the algorithm of the compiler and configuration of the processor.

In apodization, which is generally used to reduce the sidelobe components, the signal of each channel is weighted using a window function; therefore, multiplications by the number of channels are required. GCFB can be realized with a smaller number of multiplications.

Table 1 Computational load in conventional GCF, GCF_{real}, and GCFB

	GCF Multiplication	GCF Addition	GCF_{real} Multiplication	GCF_{real} Addition	GCFB Multiplication	GCFB Addition
Hilbert transform	$M(2N_f+1)$	$2MN_f$	–	–	–	–
DFT	$4M(2K_0+1)$	$2(2M-1)(2K_0+1)$	$2M(K_0+1)$	$2(M-1)(K_0+1)$	–	$2(M-1)(K_0+1)$
Numerator in Eq. (2) or (3) or (7) (without LPF)	$2(2K_0+1)$	$4K_0+1$	$2(K_0+1)$	$3K_0+1$	$2(K_0+1)$	$3K_0+1$
Denominator in Eq. (2) or (3) or (7) (without LPF)	$2M+1$	$2M-1$	$M+1$	$M-1$	–	–
LPF in Eq. (3) or (7)	–	–	$2(2N_f+1)$	$4N_f$	$2N_f+1$	$2N_f$
Total ($M=96$, $K_0=1$, $N_f=10$)	3367	3262	527	519	25	404

When baseband demodulation is used to generate the analytic signals in GCF instead of the Hilbert transform, multiplication of the mixers and LPFs for both the real (I) and imaginary (Q) parts is required, and the calculation complexity in this part increases. Instead, the calculation complexity can be reduced by lowering the sampling rate of the subsequent processing. However, regardless of whether the Hilbert transform or baseband demodulation is used, the number of calculations becomes large compared to the subsequent processing. Therefore, the total number of calculations is smaller when the analytic signal generation is omitted [28]. Second-order sampling can be used to generate approximate analytic signals with a low number of calculations, but it is not considered in the present study because it limits the sampling rate of the ADC and causes serious errors in wideband transmission [30].

Evaluation methods

Comparison of GCF_{real} and GCFB values

Because the signal binarization in the proposed method is a special process, it is difficult to express the general relationship between $S(k,n,l)$ and $U(k,n,l)$. Consequently, it is difficult to theoretically predict how the binarization process will affect the weighting of the received signal. Therefore, we focus on the effect of reducing unnecessary signals caused by sidelobes, and the ability to visualize diffused scattering media. As shown in Fig. 3, the GCF_{real} and GCFB values were compared for the following two cases using the received signal of each channel generated by simulation and acquired from a phantom using an ultrasonic diagnostic apparatus.

(a) A receiving focus region around one scatterer.

(b) A receiving focus point in a diffused scattering medium.

We evaluated the effect of binarization by comparing GCF_{real}. We used a convex probe, which is mainly used for
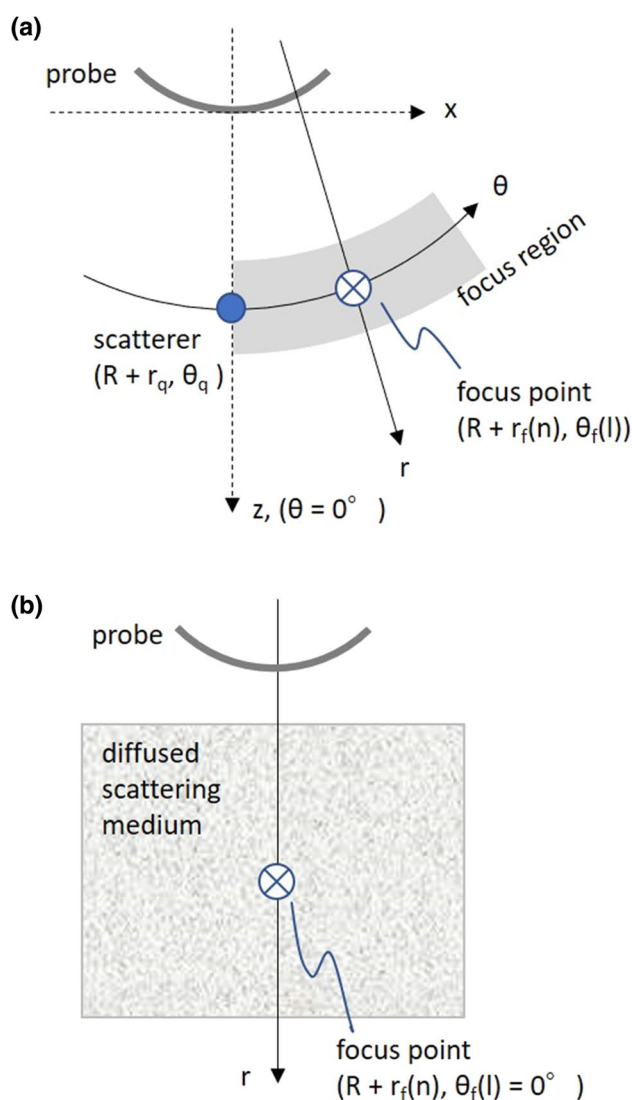

(a)

(b)

Fig. 3 Geometry for generating received signals in the simulation. **a** Receiving focus region for one scatterer. **b** Receiving focus point in a diffused scattering medium

observing the abdomen, where there are many regions of diffused scattering media.

Evaluation of B-mode images weighted by GCF$_{real}$ and GCFB

The contrast performances of B-mode images obtained with GCF$_{real}$ and GCFB were evaluated using the following contrast and CNR values:

$$Contrast = 20\log_{10}\left(\frac{\mu_1}{\mu_2}\right), \tag{8}$$

$$CNR = \frac{|\mu_1 - \mu_2|}{\sqrt{\sigma_1{}^2 + \sigma_2{}^2}}, \tag{9}$$

where μ_i and σ_i are the mean value and standard deviation of the envelope signal in region i, respectively. As shown in Eq. (1), when the GCF value is weighted to the signal after DAS, the weighting effect is adjusted by the power of p. The p-values for GCF$_{real}$ and GCFB are defined as $p_{GCFreal}$ and p_{GCFB}, respectively. $p_{GCFreal}$ is determined so that DRA does not occur near a strong scatterer. Moreover, p_{GCFB} is determined in the same region so that the mean value of GCF$_{real}$ with $p_{GCFreal}$ and that of GCFB with p_{GCFB} are equal. The contrast and CNR values are calculated from the signals of both methods adjusted by these coefficients.

Simulations and experimental setup

RF data generation by simulation

The signal change in the channel direction that occurs based on the scatterer and receiving focus positions is generated simply. As shown in Fig. 3a, b polar coordinate system $(R + r, \theta)$ is set based on the center of the curvature of the convex probe surface; here, R is the radius of the curvature of the convex probe, r is the distance from the probe surface, and θ is 0° in the vertical direction of the probe. The position of the scatterer with number q is represented by $(R + r_q, \theta_q)$.

$$r_f(n) = n/f_s \cdot c/2, \tag{10}$$

where n is the sample number in the time direction, f_s is the sampling frequency of the receiving signal, and c is the sound velocity. To consider the propagation and delay times, we converted to the Cartesian coordinate system in which the origin was set on the probe surface, the $\theta = 0°$ direction was the z axis, and the azimuth direction was the x axis, as shown in Fig. 3a. The coordinates of the scatterer (x_q, z_q) and receiving focus (x_f, z_f) are represented by

$$\begin{aligned} x_q &= (R + r_q)\sin\theta_q, \\ z_q &= (R + r_q)\cos\theta_q - R, \end{aligned} \tag{11}$$

$$\begin{aligned} x_f(n, l) &= (R + r_f(n))\sin\theta_f(l), \\ z_f(n, l) &= (R + r_f(n))\cos\theta_f(l) - R. \end{aligned} \tag{12}$$

The signal obtained by delaying the received signal from the scatterer (x_q, z_q) is represented by

$$\begin{aligned} s'(m, n, l, x_q, z_q) = \sum_{m_T=M_s}^{M_e} G\big(-\tau(m_T, m, x_q, z_q) \\ + \tau_d(m_T, m, x_{fTx}(l), z_{fTx}(l), x_f(n, l), z_f(n, l))\big), \end{aligned} \tag{13}$$

where

$$G(t) = \exp\left[-2\{\pi\sigma t\}^2\right] \cdot \cos\left[2\pi f_0 t\right] \tag{14}$$

is a Gaussian pulse with center frequency f_0 and -6 dB bandwidth σ.

$$\tau(m_T, m, x_q, z_q) = \sqrt{(x_e(m_T) - x_q)^2 + (z_e(m_T) - z_q)^2}/c + \sqrt{(x_e(m) - x_q)^2 + (z_e(m) - z_q)^2}/c \tag{15}$$

is the propagation time until the sound wave transmitted from the element with a number $m_T(= M_s, M_s + 1, \ldots, M_e)$ is reflected by the scatterer (x_q, z_q) and received by the receiving element with number m.

$$\begin{aligned} &\tau_d(m_T, m, x_{fTx}(l), z_{fTx}(l), x_f(n, l), z_f(n, l)) \\ &= \sqrt{(x_e(m_T) - x_{fTx}(l))^2 + (z_e(m_T) - z_{fTx}(l))^2}/c - r_{fTx}/c + r_f(n)/c + \sqrt{(x_e(m) - x_f(n, l))^2 + (z_e(m) - z_f(n, l))^2}/c \end{aligned} \tag{16}$$

Considering the receiving focus point $(R + r_f(n), \theta_f(l))$, where $r_f(n)$ is the receiving focus distance and $\theta_f(l)$ is the azimuth angle of the l-th scanning line, $r_f(n)$ is represented by

represents the sum of the transmitting delay time given to the element with the number m_T and the receiving delay time given to the element with number $m.(x_e(m), z_e(m))$ represents the element position with number $m.r_{fTx}$ represents the transmission focus distance, and the azimuth angle of the

transmission focus is $\theta_f(l)$, which is the same as the receiving focus. The transmission focus coordinate $\left(x_{fTx}, z_{fTx}\right)$ in the Cartesian coordinate system is

$$
\begin{aligned}
x_{fTx}(l) &= \left(r_{fTx} + R\right) \sin \theta_f(l), \\
z_{fTx}(l) &= \left(r_{fTx} + R\right) \cos \theta_f(l) - R.
\end{aligned}
\tag{17}
$$

As shown in Fig. 3b, when focusing on a diffused scattering medium, the delayed signals are generated by superimposing the received signals from Q scatterers at different positions as follows:

$$
s_{sim}(m, n, l) = \sum_{q=1}^{Q} s'\left(m, n, l, x_q, z_q\right).
\tag{18}
$$

The GCF_{real} value is calculated by substituting the real signal $s_{sim}(m, n, l)$ into $s(m, n, l)$ in Eq. (3). The GCFB value is calculated from Eq. (7) after substituting $s_{sim}(m, n, l)$ into $s(m, n, l)$ in Eq. (4). In the simulation, the amplitude values of the received signals from the anechoic region are all zero. In this case, because the signal values are all $+1$ according to Eq. (4), the GCF_{real} and GCFB values are 1. To avoid this, random noise with a maximum of -40 dB relative to the amplitude of the Gaussian pulse in Eq. (14) was added to the signal for each channel. In the simulation, the same conditions were used as the experimental data acquisition conditions presented later (Table 2). The center frequency f_0 and -6 dB bandwidth σ of the Gaussian pulse were set to 3 MHz and 1.5 MHz, respectively, according to the experimental data.

Experimental RF data acquisition

The experimental RF data were acquired using the ultrasonic diagnostic system ProSound α10 (Hitachi, Tokyo, Japan) with ultrasonic multipurpose phantom 403GS-LE (Gammex, WI, USA) as the measurement object. A convex probe (UST-9130, center frequency 3.5 MHz, radius

Table 2 Input data conditions in the simulations and the experiments

Parameter	Value
Transmit	
Number of element	76
Focus depth [mm]	105
Apodization function	Hamming
Center frequency [MHz]	5
Band width [MHz]	3
Receive	
Number of element	96
Sampling frequency [MHz]	20

of curvature 60 mm, element pitch 0.38°) was used, and the number of channels was $M = 96$. In this measurement, an image was formed from 312 received scan lines in the range of a 60° viewing angle. Both the transmitting and receiving apertures for forming the scan line were set with the scan line as the center. Table 2 lists the transmitting and receiving conditions.

Results

Comparison of GCF_{real} and GCFB values for one scatterer

In the present study, all the verifications were performed under the condition of $K_0 = 1$, which was suitable for reducing unnecessary signals in a previous study [28]. Figure 4 shows the simulation data. Figure 4a–c show the values of DAS, GCF_{real}, and GCFB, respectively, where the vertical axis is the depth $r_f(n)$ and the horizontal axis is the angle $\theta_f(l)$ of the receiving focus point, when there is one scatterer at $(r_q, \theta_q) = (46.2$ mm, $0°)$. For $\theta_f(l)$, only the positive side is shown because the result is positive–negative symmetric. For DAS, the amplitude value of the envelope is displayed in decibels. Similarly, Fig. 4d–f show the values of DAS, GCF_{real}, and GCFB, respectively, when there is one scatterer at $(r_q, \theta_q) = (65.8$ mm, $0°)$, and Fig. 4g–i show those when there is one scatterer at $(r_q, \theta_q) = (85.3$ mm, $0°)$. Since GCF_{real} and GCFB are evaluation values of coherence, they are large over a wider range in the depth direction than DAS, which represents the amplitude value. In Fig. 4a, b, it can be observed that in the region where the DAS value increased because of the sidelobe, the GCF_{real} value also increased. However, this sidelobe influence was hardly observed in Fig. 4c. Similar tendencies were observed at all depths (Fig. 4d–i). These results suggest that GCFB is more effective at reducing the unnecessary signals caused by the sidelobe components than GCF_{real}.

Figure 4j shows the values of GCF_{real} and GCFB at the scatterer depth indicated by dashed line 1 in Fig. 4b. When $\theta_f(l) < 0.5°$, the phases among the channels were roughly aligned or changed slowly, so that the GCF_{real} and GCFB values were both close to 1. However, there was a region where the GCFB value was approximately 0.2 lower than that of GCF_{real}. This is because high-frequency components in the channel direction are generated in binarized signals in the case of GCFB. In addition, GCF_{real} and GCFB increase again around $\theta_f(l) = 0.4°$, because the signal is concentrated on the component of $k = 1$. Moreover, when $\theta_f(l) > 1°$, while GCF_{real} was approximately 0, GCFB fluctuated by a small value because of the influence of binarization. Figure 4k shows the GCF_{real} and GCFB
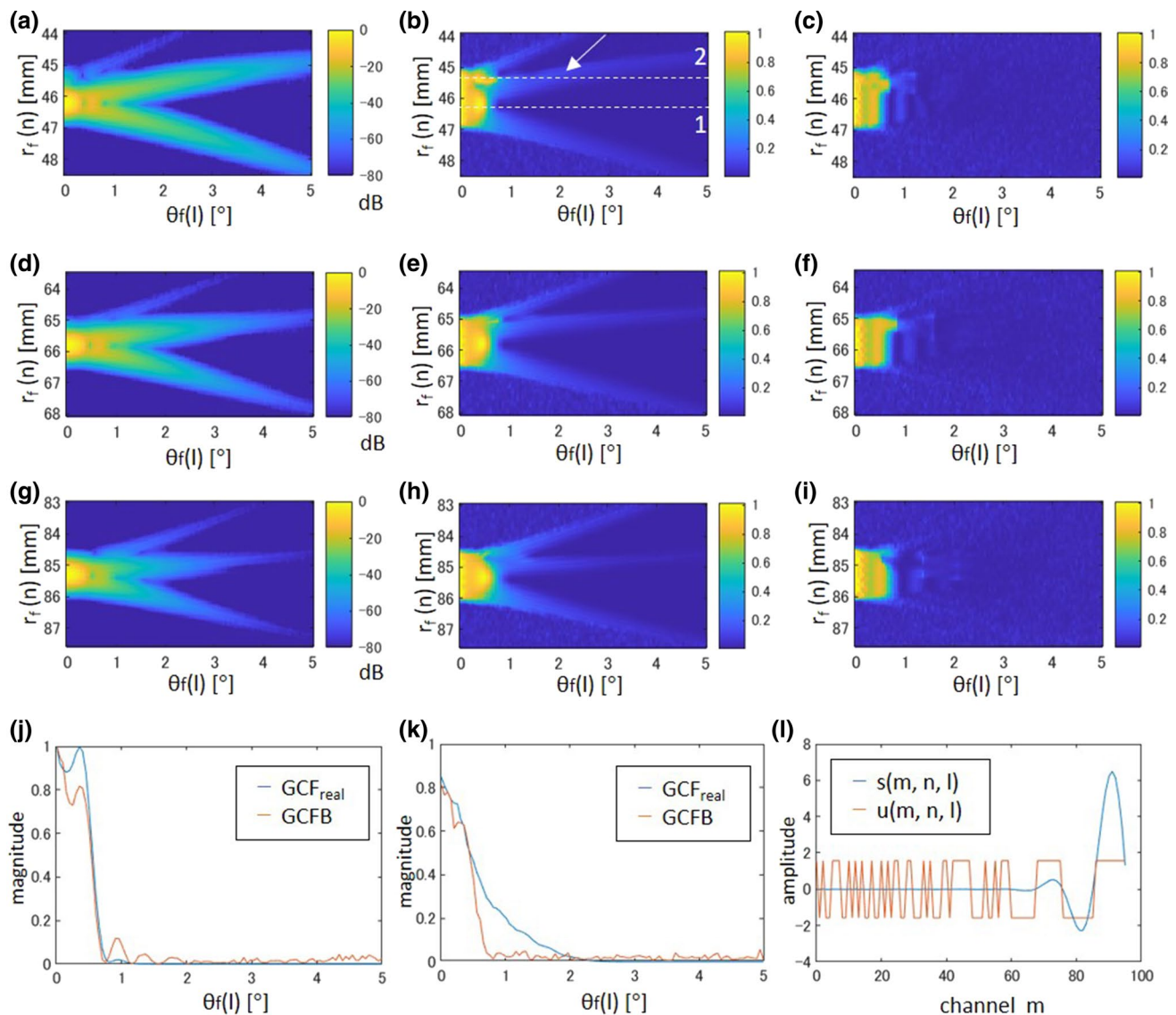
Fig. 4 Comparison of GCF$_{real}$ and GCFB values around scatterers in the simulation data. **a** DAS, **b** GCF$_{real}$, and **c** GCFB values for the scatterer at $r = 46.2$ mm. **d** DAS, **e** GCF$_{real}$, and **f** GCFB values for the scatterer at $r = 65.8$ mm. **g** DAS, **h** GCF$_{real}$, and **i** GCFB values for the scatterer at $r = 85.3$ mm. GCF$_{real}$ and GCFB values at **j** dashed line 1 and **k** dashed line 2 in **b**. **l** $s(m, n, l)$ and $u(m, n, l)$ at the position indicated by the arrow in **b**

values at the depth indicated by dashed line 2 in Fig. 4b. GCF$_{real}$ exhibited a higher value than GCFB when $\theta_f(l)$ was in the range of 0.5 to 2.0° because of the influence of the sidelobes. Figure 4l shows the real $s(m, n, l)$ and binarized $u(m, n, l)$ signals in the channel direction at the position affected by the sidelobe indicated by the arrow in Fig. 4b. Here, the amplitude values of $u(m, n, l)$ were normalized so that the power values of both signals were equal. In $s(m, n, l)$ used to calculate GCF$_{real}$, the received signal from the scatterer was dominant in the channel of $m > 60$. The GCF$_{real}$ value increased because of this signal, and the sidelobe component was not sufficiently reduced.

Figure 5a is a B-mode image constructed from the obtained experimental data. The GCF$_{real}$ and GCFB values around the three wires surrounded by yellow squares are shown in Fig. 5b–g. The vertical axis is the depth $r_f(n)$, and the horizontal axis is $\theta'_f(l)$, where the azimuth angle relative to the scanning line passing through each wire (0°) is shown as $\theta'_f(l)$. Figure 5b, c show the GCF$_{real}$ and GCFB values around the wire at $r = 46.2$ mm, Fig. 5d, e show the values at $r = 65.8$ mm, and Fig. 5f, g show the values at $r = 85.3$ mm.

Figure 5h shows the GCF$_{real}$ and GCFB values at dashed line 1 shown in Fig. 5b. Similar to the simulation results, GCFB was slightly lower than GCF at $\theta'_f(l) < 0.5°$, where
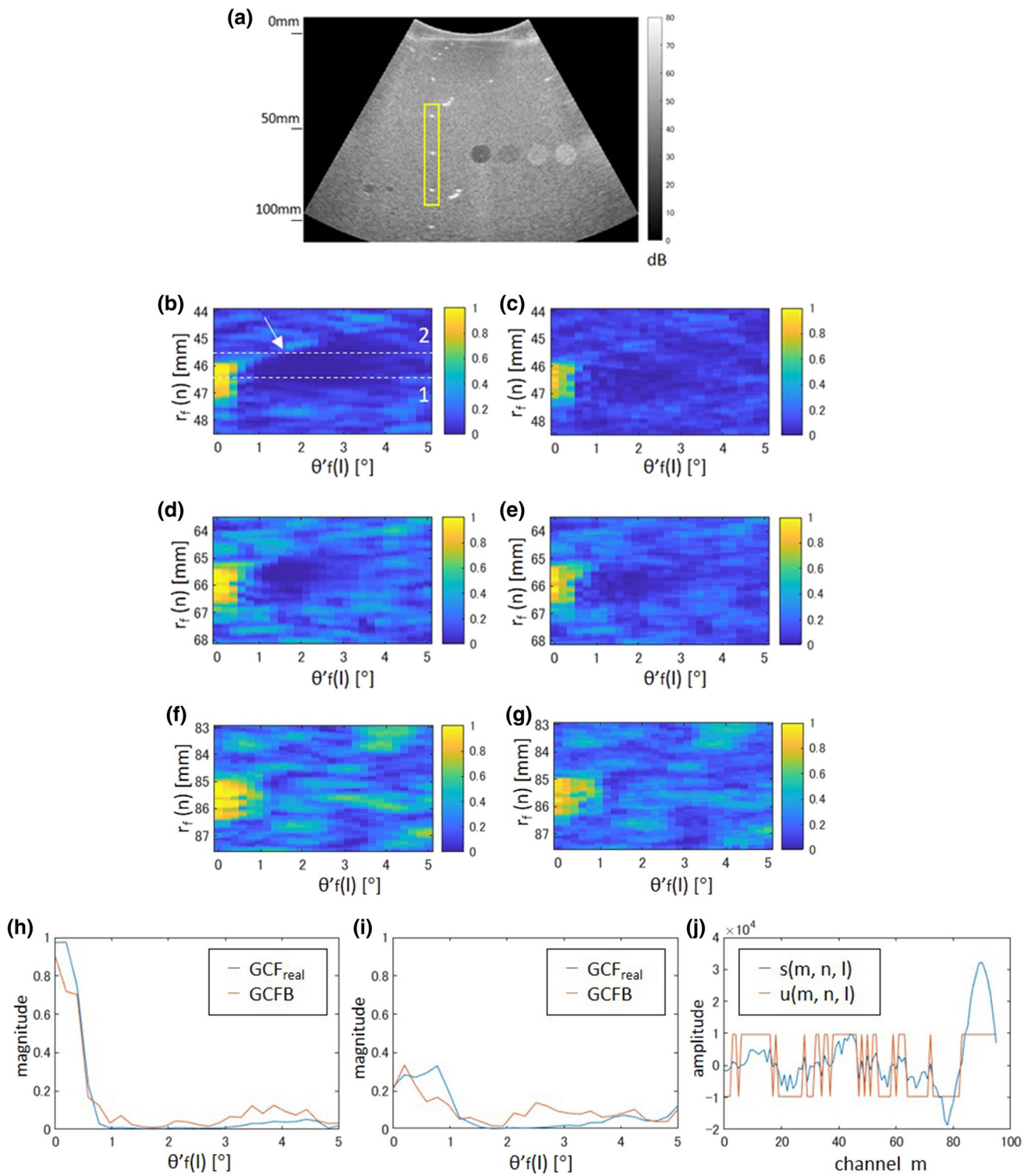
Fig. 5 Comparison of GCF$_{real}$ and GCFB values around wire targets in the experimental data. **a** B-mode image of the data. **b** GCF$_{real}$ and **c** GCFB values for the wire at $r = 46.2$ mm. **d** GCF$_{real}$ and **e** GCFB values for the wire at $r = 65.8$ mm. **f** GCF$_{real}$ and **g** GCFB values for the wire at $r = 85.3$ mm. GCF$_{real}$ and GCFB values at **h** dashed line 1 and **i** dashed line 2 in **b**. **j** $s(m, n, l)$ and $u(m, n, l)$ at the position indicated by the arrow in **b**

the signal coherence was high. GCF_{real} was approximately 0 at $1° < \theta'_f(l) < 3°$. When the signal after DAS is weighted using this value, the amplitude is significantly reduced and a DRA occurs. However, the value of GCFB was slightly larger than that of GCF_{real} in this region, which suppressed the occurrence of DRA. Figure 5i shows the GCF_{real} and GCFB values at dashed line 2 in Fig. 5b. Similar to the simulation results, it can be confirmed that GCF_{real} was large because of the influence of the sidelobe components at $0.5° < \theta'_f(l) < 1°$. Figure 5j shows the real $s(m, n, l)$ and binarized $u(m, n, l)$ signals at the positions affected by the sidelobe indicated by the arrows in Fig. 5b. Similar to Fig. 4l, the amplitude values of $u(m, n, l)$ were normalized so that the power values of both signals were equal. Similar to the simulation results, in the case of GCF_{real}, the received signal from the wire was dominant in the channel at the end ($m > 70$).

Comparison of GCF_{real} and GCFB values for diffused scattering media

Figure 6a shows the GCF_{real} and GCFB values at the receiving focus points in the diffused scattering media in the simulation data. The scatterer density was set to $100/mm^2$ to generate sufficiently dense scatterers with respect to the wavelength (0.5 mm). The mean value after repeating the simulation 100 times by changing the arrangement of the scatterers at each depth is shown. The GCF_{real} and GCFB values changed depending on the depth and increased near the transmission focus depth (105 mm). This is because the influence of the signals from the scatterers near the focus point was more dominant as the transmission beam width became narrower, and the coherence of the signals among the channels increased. The GCFB values were smaller than the GCF_{real} values, and when they were used as the weight values, the brightness of the diffused scattering media was lower than that of GCF_{real}.

Figure 6b shows the GCF_{real} and GCFB values when the noise level given to each channel was changed at $r_f(n) = 100$ mm in a diffused scattering medium. The noise level is
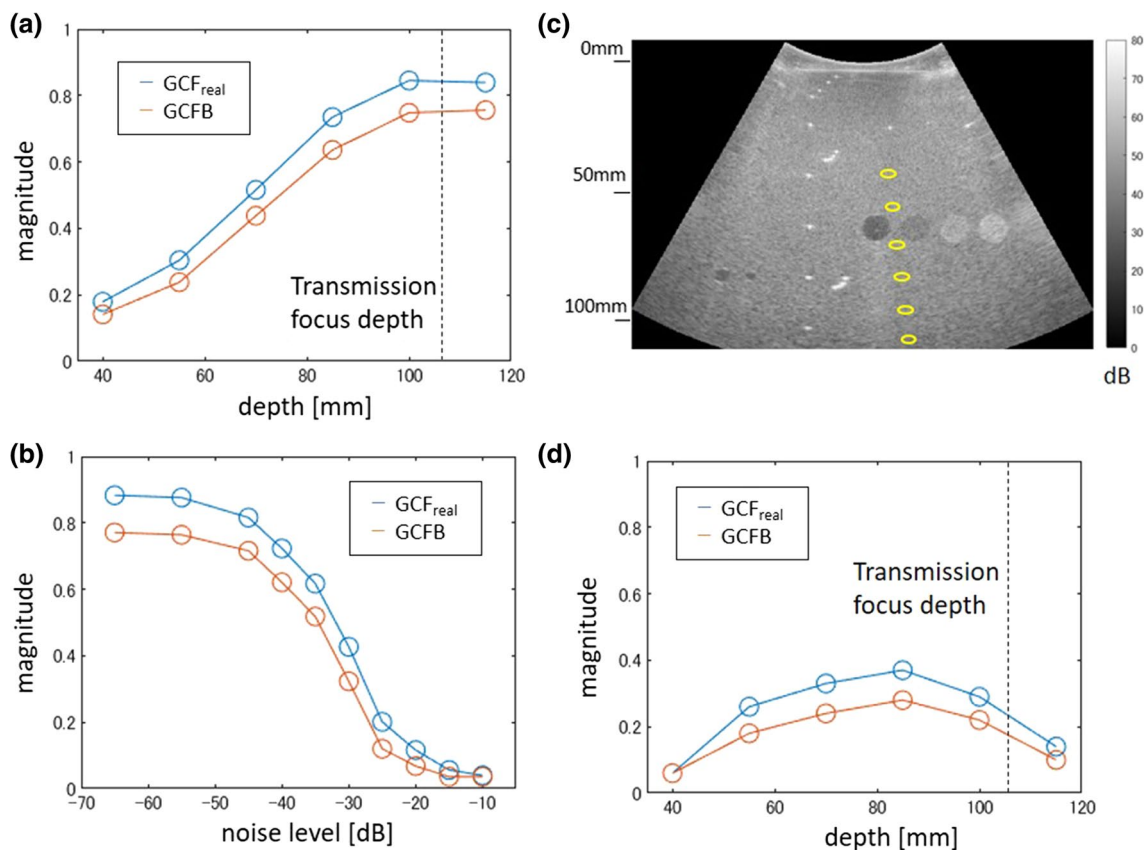

Fig. 6 Comparison of GCF_{real} and GCFB at diffused scattering medium. **a** GCF_{real} and GCFB values in the diffused scattering medium for the simulation data. **b** Changes in GCF_{real} and GCFB values relative to the noise level. **c** Regions for estimating GCF_{real} and GCFB values for the experimental data. **d** GCF_{real} and GCFB values in diffused scattering media shown in **c**

expressed as the mean value of DAS in the absence of noise as 0 dB. The values of GCF_{real} and GCFB decreased with the increase in noise level, making the difference between the two small.

The results of the experimental data are shown in Fig. 6c, d. Figure 6c is a B-mode image constructed by DAS. The mean GCF_{real} and GCFB values calculated for each region indicated by the yellow circles are shown in Fig. 6d. Similar to the simulation results, the GCFB values were smaller than the GCF_{real} values. It can also be confirmed that the difference between the GCF_{real} and GCFB values decreased as the values decreased. In the experimental data, because the SNR decreased as a result of attenuation with depth, the GCF_{real} and GCFB values were smaller than the simulation results in Fig. 6a, and were highest at 85 mm shallower than the transmission focus.

B-mode images and CNR values by CBB

Figure 7a–c show the B-mode images yielded by DAS and CBB using GCF_{real} and GCFB, obtained from the acquired experimental data. The dynamic range of the display was 80 dB. For GCF_{real}, $p_{GCFreal}$ was set to 0.2 to avoid the

Table 3 Contrast and CNR values of the B-mode image generated using each method

		DAS	GCF_{real}	GCFB
Region 1: red	Contrast [dB]	− 13.9	− 17.7	− 17.9
Region 2: yellow	CNR	2.47	2.87	2.92
Region 1: green	Contrast [dB]	− 5.2	− 7.9	− 7.8
Region 2: yellow	CNR	0.98	1.38	1.35

occurrence of DRA around the wire indicated by the arrow in Fig. 7a. As a result of adjusting p_{GCFB} so that the mean value of GCFB in the region near the wire was similar to that of GCF_{real}, p_{GCFB} was set to 0.26. Figure 7b, c show the images adjusted using these p-values. Moreover, Fig. 7d shows the azimuth brightness profile of each image averaged in the depth direction for the region shown by the yellow square in Fig. 7b. In the case of GCF_{real} and GCFB, the brightness of the diffused scattering medium was lower than that of DAS, but more than that, the brightness of the anechoic region was significantly reduced owing to the unnecessary signal reduction effect. Table 3 shows the contrast and CNR values of each image calculated from Eqs. (8) and (9), with the red and yellow squares shown in Fig. 7a
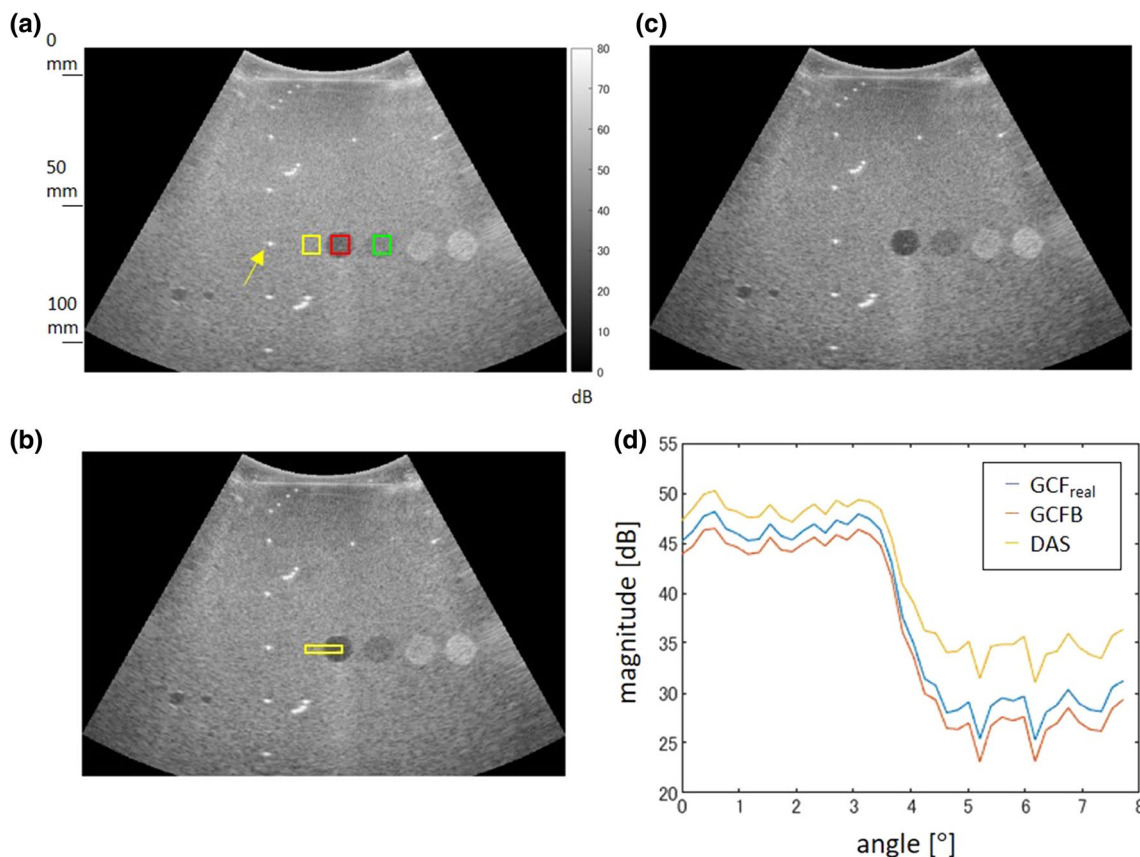

Fig. 7 B-mode images generated by **a** DAS and those weighted by **b** GCF_{real} and **c** GCFB. **d** Lateral profiles of the anechoic region shown by the square in **b**

as regions 1 and 2, and with the green and yellow squares shown in Fig. 7a as regions 1 and 2, respectively. In the case of GCF$_\text{real}$ and GCFB, both the contrast and CNR were superior to DAS, and the same degree of contrast improvement was observed.

Discussion

The advantages of GCFB over GCF$_\text{real}$ are discussed below. For signals such as those shown in Figs. 4l and 5j, positive signals near $m = 90$, which are considered to be signals from the strong scatterer around the receiving focus point, are dominant. Consequently, the DAS value increases even though there is no scatterer at the focus point. This is the influence of the sidelobe component. In this case, because the DC component increases, the numerator of Eq. (3) also increases, making the GCF$_\text{real}$ value large and similar to that of DAS. However, in the case of GCFB calculated from the binarized signal $u(m, n, l)$, the amplitude value of the signal is not considered, and the signal received by more channels becomes dominant. For example, for the signal shown in Fig. 4l, because there is no scatterer at the receiving focus point, all signals at $m < 60$, which are not signals from the scatterer, are noise. Because the GCFB uses binarization, these noise signals become dominant. The effect is relatively weak because the number of receiving channels is small for signals near $m = 90$. Consequently, the GCFB value is smaller than that of GCF$_\text{real}$, which considers the amplitude, at the position where the sidelobe component is generated in DAS. As shown in Fig. 5j, when the focus point is in a diffused scattering medium, the signals from the diffused scattering medium are received by all channels. However, some channels receive signals from the wire located at a position different from the focus point. Therefore, the calculated GCFB value is significantly influenced by the diffused scattering medium, and the influence of the sidelobe component can be relatively suppressed. From the above, when the signal caused by the sidelobe is larger than the original signal of the receiving focus point and becomes an unnecessary signal, GCFB has an excellent reduction effect compared to GCF$_\text{real}$.

Similarly, even in the vicinity of a strong scatterer where DRA is likely to occur, the influence of the signal from the focus point is stronger than that from the strong scatterer at a position different from the focus point in GCFB. Therefore, the value does not decrease as significantly as GCF$_\text{real}$, and GCFB suppresses the occurrence of DRA more than GCF$_\text{real}$.

From the above, GCFB is superior to GCF$_\text{real}$ in reducing unnecessary signals and can suppress the occurrence of DRA. The wider the bandwidth, the fewer the channels that receive the signal from the strong scatterer, and the stronger this tendency becomes. This feature generally holds regardless of the measurement target.

The disadvantages of GCFB versus GCF$_\text{real}$ are discussed below. As can be observed in Figs. 4j and 5h, both GCFB and GCF$_\text{real}$ have values close to 1 near $\theta_\text{f}(l) = 0°$, where the receiving focus and scatterer position match. However, in the vicinity of $\theta_\text{f}(l) = 0.3°$, where the receiving focus is slightly shifted from the scatterer, a slight phase change occurs in the signal in the channel direction. High-frequency components are generated in the frequency spectrum in the channel direction by binarizing the signal, such that GCFB has a smaller value than GCF$_\text{real}$. The advantage of GCF is that it becomes a large value and the brightness can be maintained even when there is a slight phase change, whereas GCFB may reduce such signals. However, if $p < 1$ is adjusted so that DRA does not occur in GCF, a larger GCF value leads to a smaller change in $[GCF(n, l)]^p$ with regards to the change in the GCF value, as shown in Fig. 1b. Therefore, for a signal with high coherence, even if there is a slight difference between the GCFB and GCF$_\text{real}$ values, the difference between the two after adjustment with the p-values (< 1) is small, having a slight effect on the image quality.

Similarly, for a signal from the diffused scattering medium, as a result of the scattered waves interfering with each other, a phase change occurs in the channel direction [6], and high-frequency components increase because of binarization. Therefore, as shown in Fig. 6a, d, GCFB has smaller values than GCF$_\text{real}$, which may reduce the brightness. Because the GCFB value in the diffused scattering medium is not as large as the GCFB value at the strong scatterer, the brightness value decreases, as shown in Fig. 7d, even if it is adjusted by the p-value.

As mentioned above, GCFB is superior to GCF$_\text{real}$ in terms of its ability to reduce unnecessary signals generated by sidelobes; however, the brightness value of the diffused scattering medium is also reduced. Consequently, the contrast and CNR calculated from the diffused scattering medium and the hypoechoic regions are equivalent to those of GCF$_\text{real}$, as shown in Table 3. However, because the contrast and CNR depend on the degree of reduction in brightness in the diffused scattering medium and the degree of reduction in unnecessary signals, the performances of GCFB and GCF$_\text{real}$ are considered to depend on the observation target.

Additionally, since GCF is a process that reduces the brightness of unnecessary signals, the resolution of an image generated using GCF is not inferior to that of DAS. However, since the noise component is also reduced, it may give the impression that spatial high-frequency components are suppressed.

Table 4 Relationship between coherence factors

Input signal	Only the DC component	Components around DC
Real signal	CF, i.e. GCF ($K_0 = 0$)	GCF ($K_0 > 0$)
Binarized signal	SCF, i.e. GCFB ($K_0 = 0$)	GCFB ($K_0 > 0$)

In the present study, to evaluate the effect of binarization, GCFB was verified with GCF_{real} as a comparator. Because GCF and GCF_{real} have equivalent values [28], it is considered that the same results can be obtained by comparing GCF and GCFB. In the case of the sign coherence factor (SCF) [8], which is one of the coherence factors, the phase of the signal is binarized to 0° and 180° in calculating the phase coherence factor (PCF) [8], which indicates the variance value of the phase in the channel direction. Similar to the proposed method, the phase variance value is calculated using the mean value of the binarized signals. It is considered that SCF and GCFB ($K_0 = 0$) are similar because the process of calculating the variance value from the mean value of binarized signals is considered to be similar to adjusting the effect (a conversion such as the *p*-value). Table 4 summarizes these relationships, and SCF using binarized signals is a special case of GCFB ($K_0 = 0$). By evaluating up to the DC vicinity component ($K_0 > 0$) in GCF, the variation in values can be suppressed in diffused scattering media, and CNR values superior to CF and SCF can be obtained. This effect can also be achieved with GCFB.

Conclusions

In the present study, we proposed a GCFB that binarizes the input real signals to reduce the number of GCF computations. Focusing on the effect of reducing unnecessary signals and the ability to visualize diffused scattering media, the validity of the proposed method was verified using simulation and experimental data. From the results, the contrast performance was superior to DAS in the case of both the conventional method and GCFB. The performance of both methods for improving the CNR may depend on the observation target. Under the conditions in the present study, comparable performance was achieved with both methods. Because GCFB can significantly reduce the computational complexity by binarization, it is potentially applicable for clinical diagnostic equipment.

Declarations

References

1. Mohamed SA, Mohamed ED, Elshikh MF, et al. Design of digital apodization technique for medical ultrasound imaging. Int Conf Comput Electr Electron Eng. 2013.
2. Capon J. High-resolution frequency-wavenumber spectrum analysis. Proc IEEE. 1969;57:1408–18.
3. Synnevag JF, Austeng A, Holm S. Adaptive beamforming applied to medical ultrasound imaging. IEEE Trans Ultrason Ferroelectr Freq Control. 2007;54:1606–13.
4. Synnevag JF, Austeng A, Holm S. Benefits of minimum-variance beamforming in medical ultrasound imaging. IEEE Trans Ultrason Ferroelectr Freq Control. 2009;56:1868–79.
5. Hollman KW, Rigby KW, O'Donnell M. Coherence factor of speckle from a multi-row probe. Proc IEEE Ultrason Symp. 1999;2:1257–60.
6. Li PC, Li ML. Adaptive imaging using the generalized coherence factor. IEEE Trans Ultrason Ferroelectr Freq Control. 2003;50:128–41.
7. Wang SL, Chang CH, Yang HC, et al. Performance evaluation of coherence-based adaptive imaging using clinical breast data. IEEE Trans Ultrason Ferroelectr Freq Control. 2007;54:1669–78.
8. Camacho J, Parrilla M, Fritsch C. Phase coherence imaging. IEEE Trans Ultrason Ferroelectr Freq Control. 2009;56:958–74.
9. Wang Y, Zheng C, Peng H, et al. An adaptive beamforming method for ultrasound imaging based on the mean to standard deviation factor. Ultrasonics. 2018;90:32–41.
10. Hasegawa H, Kanai H. Effect of sub-aperture beamforming on phase coherence factor imaging. IEEE Trans Ultrason Ferroelectr Freq Control. 2014;61:1779–90.
11. Sakhaei SM. Optimum beamforming for sidelobe reduction in ultrasound imaging. IEEE Trans Ultrason Ferroelectr Freq Control. 2012;59:799–805.
12. Nilsen CIC, Holm S. Wiener beamforming and the coherence factor in ultrasound imaging. IEEE Trans Ultrason Ferroelectr Freq Control. 2010;57:1329–46.
13. Kanai H, Sato M, Koiwa Y, et al. Transcutaneous measurement and spectrum analysis of heart wall vibrations. IEEE Trans Ultrason Ferroelectr Freq Control. 1996;43:791–810.
14. Mallart R, Fink M. Adaptive focusing in scattering media through sound-speed inhomogeneities: The van Cittert Zernike approach and focusing criterion. J Acoust Soc Am. 1994;96:3721–32.
15. Burckhardt CB. Speckle in ultrasound B-mode scans. IEEE Trans Son Ultrason. 1978;25(1):1–6.
16. Wagner RF, Smith SW, Sandrik JM, et al. Statistics of speckle in ultrasound B-scans. IEEE Trans Son Ultrason. 1983;30:156–63.
17. Patterson MS, Foster FS. The improvement and quantitative assessment of B-mode images produced by an annular array/cone hybrid. Ultrason Imag. 1983;5:195–213.
18. Shen CC, Xing YQ, Jeng G. Autocorrelation based generalized coherence factor for low-complexity adaptive beamforming. Ultrasonics. 2016;72:177–83.
19. Hverven SM, Rindal OMH, Rodriguez-Molares A, et al. (2017) The influence of speckle statistics on contrast metrics in ultrasound imaging. IEEE Ultrason Symp 1–4
20. Tanter M, Fink M. Ultrafast imaging in biomedical ultrasound. IEEE Trans Ultrason Ferroelectr Freq Control. 2014;61:102–19.
21. Yiu BYS, Tsang IKH, Yu ACH. GPU-based beamformer: Fast realization of plane wave compounding and synthetic

aperture imaging. IEEE Trans Ultrason Ferroelectr Freq Control. 2011;58:1698–705.

22. Bae MH, Jeong MK. A study of synthetic-aperture imaging with virtual source elements in B-mode ultrasound imaging systems. IEEE Trans Ultrason Ferroelectr Freq Control. 2000;47:1510–9.

23. Frazier CH, O'Brien WD. Synthetic aperture techniques with a virtual source element. IEEE Trans Ultrason Ferroelectr Freq Control. 1998;45:196–207.

24. Rasmussen JH, Hemmsen MC, Madsen SS, et al. (2012) Implementation of tissue harmonic synthetic aperture imaging on a commercial ultrasound system. IEEE Intl Ultrasound Symp 121–125

25. Nikolov SI, Kortbek J, Jensen JA (2012) Practical applications of synthetic aperture imaging. IEEE Intl Ultrasound Symp 350–8

26. Karaman M, Li PC, O'Donnel M. Synthetic aperture imaging for small scale systems. IEEE Trans Ultrason Ferroelectr Freq Control. 1995;42:429–42.

27. Hasegawa H, Kanai H. High-frame-rate echocardiography using diverging transmit beams and parallel receive beamforming. J Med Ultrason. 2011;38:129–40.

28. Hisatsu M, Mori S, Arakawa M, et al. Generalized coherence factor estimated from real signals in ultrasound beamforming. J Med Ultrason. 2020;47:179–92.

29. Rindal OMH, Rodriguez-Molares A, Austeng A. (2017) The dark region artifact in adaptive ultrasound beamforming. IEEE Intl Ultrasound Symp

30. Cho WH, Ahn YB. Multi-order sampling for digital beamforming of wide-band signals. IEEE Trans Ultrason Ferroelectr Freq Control. 1996;43:495–9.